Memoirs of the Faculty of Science, Kyoto University, Series of Physics, Astrophysics, Geophysics and Chemistry, Vol.XXXXV, Article 1, 2004

Multilevel avoided crossings in high Rydberg states of ^{85}Rb

By

Kentaro Kominato

Nuclear Science Division, Institute for Chemical Research, Kyoto University
Gokasho, Uji, Kyoto 611-0011, Japan

(*Received December 6, 2003*)

Abstract

Time evolution of the $113s_{1/2}$ state of ^{85}Rb in a pulsed electric field was investigated at the region of the first avoided-crossing with its adjacent manifold. The state was initially prepared by laser excitations at a well isolated Stark position from the manifold, and driven into an electric field (F_r) over the first avoided crossing point with various slew-rates. The $s_{1/2}$ state was then field-ionized with a following high slew-rate pulsed electric field; Specifically in this field ionization process with high slew-rate regime, a constant transverse electric field was applied to enhance the tunneling field ionization process resulting from the angular momentum rotation due to the effect of a rotating electric field. Three paths through the Stark map were identified with sharp peaks in the ionization field-strength observed. One path corresponds to the autoionization-like process, while the other two paths are due to the tunneling processes with an adiabatic and a non-adiabatic transitions, respectively. Transition rates to these ionization paths, measured as a function of the slew rate, were found to be strongly dependent on how deep the state is driven into the manifold-merged region at F_r before the fast ionization-pulse was subsequently applied. Quantum theoretical predictions, taking into account explicitly the occurrence of the multilevel avoided crossings, reproduce well the experimental transition rates to the paths leading to the tunneling field-ionization. The transitions leading to the autoionization-like process, however, show different behavior from those to the tunneling process, indicating an interference effect in the process.

Contents

1 Introduction

Avoided crossings of energy levels with a time-varying external field commonly occur in many situations of research field, such as in atomic and molecular collisions[1, 2], driven charge transport in quantum dots[3], Bose-Einstein condensates[4, 5]. Transitions at a two-level avoided crossing are the basic situation for this physics and the transitions from one of the initial state to the final states are adiabatic or non-adiabatic (diabatic) ones, respectively as shown in Fig.1. The transition rates in this case have been usually treated with the Landau-Zener (LZ)[1, 2] formula in which the time-varying field is assumed to change linearly with time and evolution of the system is integrated from the infinite initial to infinite final times. For example in the Rydberg atom system, a number of authors[6] investigated experimentally the transitional behavior at an avoided crossing in alkali atoms and generally found good agreement with the prediction of the LZ formula or of its extended treatment taking into account the actual time variation of the external field different from the linearly ramped shape[6].

Extensions of the investigations to the case of multilevel avoided crossings have recently attracted much attention due to the numerous applications in various fields such as those exemplified above. One of the interesting physics along this line is the multilevel avoided crossings in highly excited Rydberg atoms: as an example, a Stark map in the vicinity of the first avoided crossing of the $113s_{1/2}$ state with adjacent manifold is shown in Fig.2. With increasing higher excited state, neighboring levels are more and more closely spaced so that their mutual interactions no more allow for their relevant crossings to be treated as a series of independent single two-level crossing. Therefore it is inevitable to take into account the effect of simultaneous occurrence of many number of level crossings (multilevel crossings) for these highly excited Rydberg states. Highly excited Rydberg atoms are one of the most ideal system for investigating the multilevel avoided crossings, since it is possible to manipulate the physical situation by suitably changing the region of applied electric field and also the excited states of Rydberg atoms. In spite of these circumstances, the multilevel avoided crossings in Rydberg atoms have not been investigated in detail experimentally as well as theoretically so far.

Besides its intrinsic interests, quantitative understanding of the multilevel avoided crossings in high Rydberg states is especially important for the achievement of strict selectivity in the pulsed field ionization scheme; A selective field-ionization scheme for the closely spaced low ℓ states through the overall adiabatic transition processes in the Stark map which has been usually adopted for the low-lying Rydberg states (for n less than 60 or so), is

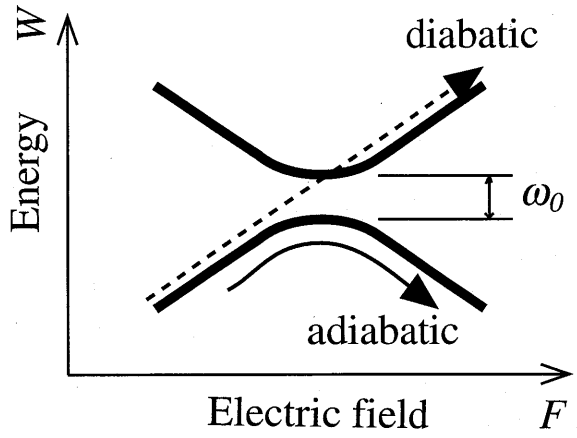

Figure 1: Two-level avoided crossing with a gap energy ω_0. When the electric field is driven slowly through the avoided crossing compared to the time of $1/\omega_0$, the passage is adiabatic (solid arrow), while driven rapidly, the passage is diabatic (broken arrow).

not quite effective for the high-lying Rydberg states, because the difference of the ionization field values between the two neighboring states is smaller and therefore very precise control of the static electric field profile in the field ionization electrodes has to be realized in addition to the fine tuning and noise-free, stable operation of the applied electric field. In order to circumvent this difficulty, a much more effective manipulation scheme for choosing a suitable ionization path on the Stark map has to be invoked. For this purpose, it is essential to know quantitatively the transitional behavior of the relevant levels at the multilevel avoided crossings.

In addition to the realization of the stringent field ionization scheme mentioned above, versatile theoretical treatment of the multilevel avoided crossings is required for the quantitative understanding of the overall time evolution of Rydberg states in a pulsed electric field. Specifically the theoretical treatment here has to be flexible enough in a sense that the calculated results should be able to compare with actual experimental results in which the experimental conditions on the external field variation and the time duration of the applied electric field are not simple to be treated by the LZ formula. In order to fulfill these requirements, it is inevitable to develop a numerical method to calculate the time evolution of the system in any arbitrary situations.

We report here the experimental results on the multilevel avoided-crossing behavior at the region of the first avoided crossing between the $113s_{1/2}$ states and the adjacent manifold. Specifically the transition of the initially populated $113s_{1/2}$ state to a splitting manifold state was investigated by subsequently ionizing the manifold states as a function of the slew rate of the applied electric field pulse. It is noted here that a definite transverse electric field was applied in the course of the pulsed field ionization process. The existence of the transverse electric field results in a rotating electric field of the field ionization processes and thus brings a change of the total angular momentum of the initially populated $s_{1/2}$ state and enhances the occurrence of the tunneling ionization process. This enhancement of the tunneling process allows us to clearly distinguish the two ionization paths leading to the adiabatic and diabatic ionizations.

It was found from the present measurements that when the slew rate of the pulse is low, the $s_{1/2}$ state moves to the lowermost (reddest) state of the manifold via an adiabatic transition, while with increasing slew rate, the state passes through many splitting states in the manifold intermediately and finally takes the non-adiabatic path. The transitions therefore depend strongly on the electric field F_r reached before a high slew-rate ionizing field is applied. Along with the experimental investigations, we performed a numerical calculation on the multilevel avoided crossings and compared the theoretical predictions thus obtained with the experimental results. In this treatment arbitrary electric field pulse shape can be applied for an arbitrary time duration so that the time evolution of the system can be picked up at an appropriate time to follow the actual experimental situations without any crude approximations. The present quantum theoretical calculations on the transitions leading to the tunneling processes, which takes into account the effect of the multilevel avoided crossings explicitly, are in good agreement with the experimental results. However, the transition to the autoionization-like process shows different behavior from those to the tunneling processes, indicating thus some interference effect on the transitions.

In the following sections, the experimental results as well as theoretical calculations are described together with the experimental setup, apparatus and comparison between the experimental results and the theoretical predictions. Following the general remarks on the Rydberg atoms in the next section, theoretical treatments in the present study are described in section 3. In section 4 the experimental setup and apparatus are presented in somewhat detail, and then experimental results and their comparisons with theoretical predictions are discussed in section 5. The final section is devoted to the conclusion of the present investigations.

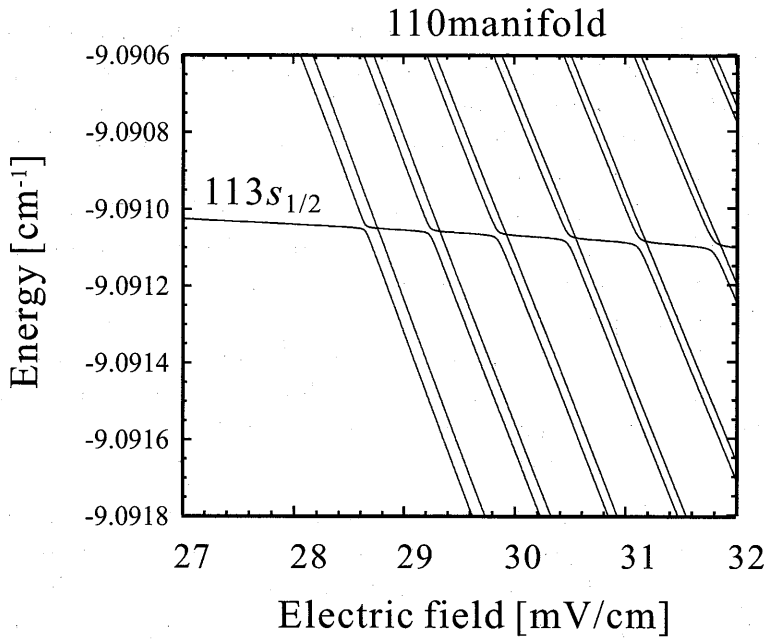

Figure 2: Close view of a Stark map around the first avoided crossing of the $113s_{1/2}$ state with the adjacent n=110 manifold states.

2 Rydberg atoms and field ionization

2.1 Overview

Rydberg atoms are the highly excited atoms near to the ionization limit with a large principal quantum number n. The binding energy of non-hydrogenic alkali atoms is given by the Rydberg formula,

$$W_{n\ell} = R/(n-\delta_\ell)^2 = R/n^{*2}, \tag{1}$$

where R is the Rydberg constant, 13.6 eV, δ_ℓ is the quantum defect of the states with angular momentum ℓ and $n^* = n - \delta_\ell$ is the effective quantum number. For low ℓ states, the penetration and polarization of the ionic core by the valence electron lead to large quantum defects and to strong departures from the hydrogenic behavior. As ℓ increases, the orbit of the valence electron becomes more circular and the atom becomes more hydrogenic.

The Rydberg atoms have following characteristics: 1) Small energy differences between the n and $n+1$ levels; the energy difference between the adjacent Rydberg states is given by $\Delta W_n = W_{n+1} - W_n \approx R/n^{*3}$ and lies

mostly in the microwave range. In the case of $n \sim 100$, for example, the transition frequency is around 7 GHz. 2)Large $E1$ transition rates between the n and $n+1$ levels; the Rydberg atom strongly couples to the electromagnetic field in the microwave range. The dipole matrix element is proportional to n^2;

$$q < nl|r|n'l' > \propto n^2, \tag{2}$$

where q is the electron charge. The transition probability is thus proportional to n^4;

$$q^2 < nl|r|n'l' >^2 \propto n^4. \tag{3}$$

The transition rate in vacuum between the n and $n+1$ states is approximately

$$\Gamma_n \left(\sec^{-1}\right) \approx 10^5 n^{*4} \left(\Delta W_n \left(\mathrm{eV}\right)\right)^3. \tag{4}$$

In the case of $n \sim 100$, the rate is estimated to be 3×10^4 sec^{-1}. 3)Long lifetimes; The radiative life time $\tau_{n\ell}$ of n state with low ℓ is proportional to n^3, while for $\ell \sim n$, it is proportional to n^5. Total decay rate $1/\tau^T_{n\ell}$ is then given by

$$\frac{1}{\tau^T_{n\ell}} = \frac{1}{\tau_{n\ell}} + \frac{1}{\tau^{bb}_{n\ell}}, \tag{5}$$

where $\tau^{bb}_{n\ell}$ is the radiative life time induced by the blackbody radiation given by

$$\tau^{bb}_n = 2.03 \times 10^{-7} (n^*)^2 \frac{300\,\mathrm{K}}{T}. \tag{6}$$

The lifetime at room temperature for the state with $n \sim 100$ is estimated to be 2 msec.

2.2 Stark structure

2.2.1 Hydrogen atom

The most straightforward way to treat the Stark effect in the hydrogenic atom is to use parabolic coordinates, in which the problem remains separable even with an electric field. In the electric field F, the potential term is given by

$$V(r) = -\frac{1}{r} + Fz. \tag{7}$$

In parabolic coordinates the Shrödinger equation for an electron in the potential of Eq. (7) can be separated as,

$$\Psi(\xi, \eta) = \frac{1}{\sqrt{\xi\eta}} \Xi(\xi) H(\eta), \tag{8}$$

$$\frac{d^2\Xi(\xi)}{d\xi^2} - \left(\frac{m^2-1}{4\xi^2} - \frac{Z_1}{\xi} - \frac{W}{2} + \frac{F}{4}\xi\right)\Xi(\xi) = 0, \tag{9}$$

$$\frac{d^2H(\eta)}{d\eta^2} - \left(\frac{m^2-1}{4\eta^2} - \frac{Z_2}{\eta} - \frac{W}{2} - \frac{F}{4}\eta\right)H(\eta) = 0, \tag{10}$$

where Z_1 and Z_2 are the separation constants and both are related by $Z_1 + Z_2 = 1$. With the first order perturbation, the energy of the Rydberg state in the electric field is expressed as,

$$W_{nn_1n_2m} = -\frac{1}{2n^2} + \frac{3}{2}Fn(n_1 - n_2), \tag{11}$$

where n_1 and n_2 are the parabolic quantum numbers and related to the principal quantum number n and the magnetic quantum number m by

$$n = n_1 + n_2 + |m| + 1. \tag{12}$$

Equation (11) shows that the states with n in zero field split into $(n - 1 - |m|)$ levels in an electric field. The set of $(n-1-|m|)$ degenerated states is called "manifold". The states with higher energy in a manifold, *i.e.* the states with $n_1 - n_2 \geq 0$, are called "blue" states, and those with $n_1 - n_2 \leq 0$ are called "red" states.

The quantum number n_1 and n_2 are related to the separation parameters,

$$Z_1 = \frac{1}{n}\left(n_1 + \frac{|m|+1}{2}\right), \tag{13}$$

$$Z_2 = \frac{1}{n}\left(n_2 + \frac{|m|+1}{2}\right). \tag{14}$$

We use the difference of the separation parameters $Z_1 - Z_2$ to express the energy level in manifold. For the bluest, the central and the reddest states with $n_1 - n_2 \sim +n$, 0 and $-n$, the value of $Z_1 - Z_2$ has $\sim +1$, 0 and -1, respectively. The Stark structure of a hydrogenic atom is shown in Fig. 3.

With increasing field strength, the bluest state with n cross with the reddest state with $(n+1)$. The crossing occurs at the field strength,

$$F = \frac{1}{3n^5} = 0.17\left(\frac{100}{n}\right)\text{V/cm}. \tag{15}$$

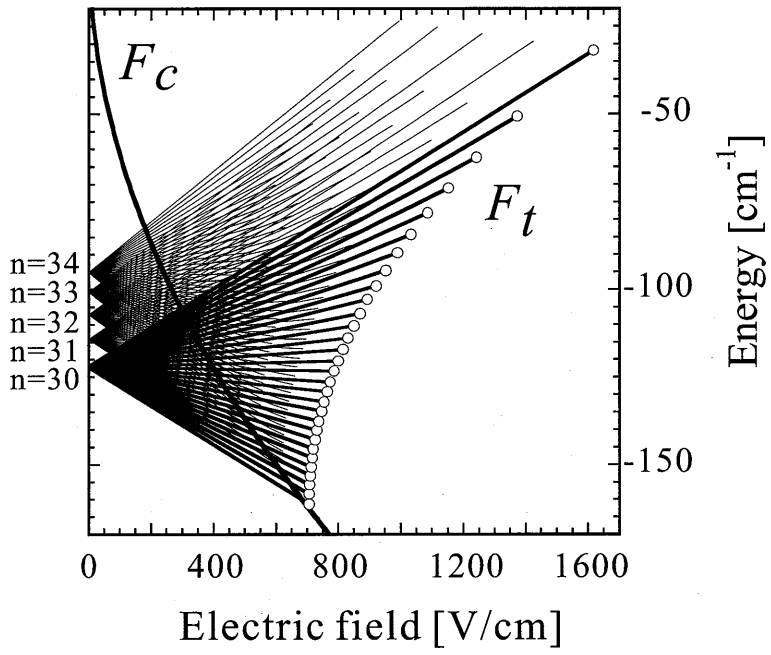

Figure 3: Part of typical Stark energy map of hydrogenic atoms. F_c represents the classical saddle-point field value, while the open circles denoted F_t show the ionization field values expected from the tunneling ionization process.

2.2.2 Non-hydrogenic atoms

Non-hydrogenic atoms have characteristics essentially similar to those of hydrogen atom in an electric field, but there are important differences due to the presence of the finite-sized ionic core.

In this situation, Hamiltonian is represented as

$$H = -\frac{1}{r} + Fz + V_d(r), \tag{16}$$

where V_d is the difference from the hydrogen potential due to the finite ionic core. The matrix element of V_d within the same n-state is given by

$$< n\ell m|V_d(r)|n\ell m >= \frac{\delta_\ell}{n^3}. \tag{17}$$

Because of the spherical symmetry of $V_d(r)$, this operator does not change ℓ and m. The matrix element between states with different n takes a finite

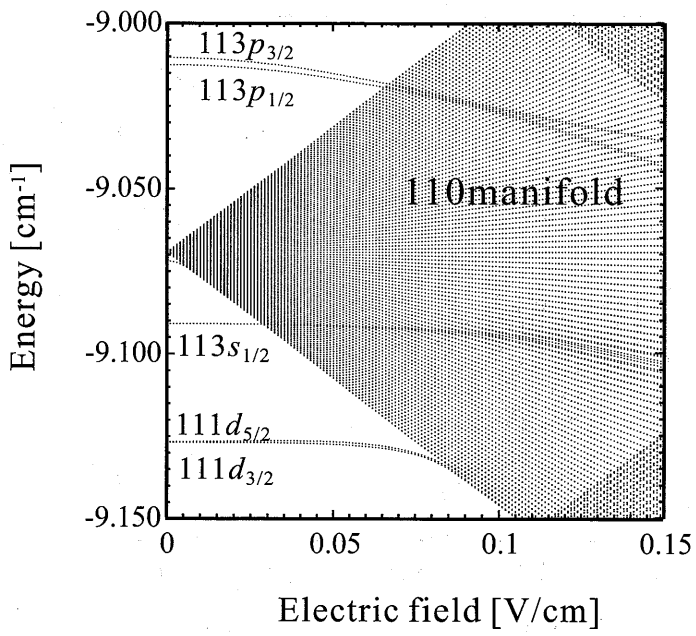

Figure 4: Stark energy level diagram around the n=110 manifold in ^{85}Rb.

value,

$$< n\ell m|V_d(r)|n'\ell m >= \frac{\delta_\ell}{\sqrt{n^3 n'^3}}. \tag{18}$$

In the representation of parabolic states, it is given by

$$< nn_1n_2m|V_d|n'n_1'n_2'm >= \sum_\ell < nn_1n_2m|n\ell m > \frac{-\delta_\ell}{\sqrt{n^3n'^3}} < n'\ell m|n'n_1'n_2'm > . \tag{19}$$

For heavier atoms such as Rb and Cs, the effect of spin-orbit force can not be neglected. In this case the Hamiltonian is

$$H = -\frac{1}{r} + Fz + V_d(r) + \Lambda. \tag{20}$$

Contrary to the case of hydrogen atom, the diagonalization of Eq.(20) can not be achieved analytically. Therefore we have to solve it numerically. While splitting manifold states shift almost linearly with electric field, s, p and d states shift quadratically in energy[7].

Figure 4 shows the energy diagram of ^{85}Rb around $n = 110$ manifold with $|m_j| = 1/2$ in an electric field.

It is noted that the degeneracy of low ℓ states, the s, p and d states, is resolved even in zero field, and the p state locates above the manifold and the s and d states below the manifold in ^{85}Rb. The second effect of the presence of the finite-sized ionic core (*i.e.* the presence of the nonzero quantum defects) is that n_1 is not a good quantum number and blue and red states are coupled with each other by the overlap at the core. When the field strength reaches $1/3n^5$, blue and red states with adjacent n do not cross with each other, but exhibit an avoided crossing.

2.2.3 Avoided crossings

Avoided crossings appearing in the Stark map of non-hydrogenic atoms affect the time evolution of the system in a pulsed electric field. If the crossing is traversed fast compared to the inverse of the separation energy between the states, $1/\omega_0$, the traversal is non-adiabatic as shown in Fig.1. The probability of the non-adiabatic transition in an isolated two level system is usually treated by the Landau-Zener formula,

$$P = \exp(-2\pi \frac{S_x}{S}). \tag{21}$$

Here S_x is defined by

$$S_x = \frac{\omega_0^2}{\left(\frac{dW_1}{dF} - \frac{dW_2}{dF}\right)}, \tag{22}$$

where dW_1/dF and dW_2/dF are the Stark shifts for each level and S is the time differential of the electric field, $S = dF/dt$. Here the time-varying field is assumed to change linearly with time and evolution of the system is integrated from the infinite initial to infinite final times. A more refined treatment to take into account the non-linear field changing was discussed by Rubbmark et al.[6].

2.2.4 Field ionization

The binding energy of a valence electron decreases as n^{-2} and thus with increasing n, the Rydberg states are strongly affected by the external electric field owing to the large dipole moment. The potential $V(r)$ has a saddle point at $z = 1/\sqrt{F}$, at which the potential value is

$$V_{\max} = -2\sqrt{F}. \tag{23}$$

If the electron is bound by an energy W, a field given by

$$F = \frac{W^2}{4} \tag{24}$$

is adequate for the ionization to occur classically. This field value is usually termed the classical saddle-point field for ionization. Ignoring the energy shift in the electric field, W is given by $-1/2n^2$, then we obtain the result,

$$F_c = \frac{1}{16n^4} = 3.2 \times \left(\frac{100}{n}\right)^4 \text{V/cm}. \tag{25}$$

This classical picture is useful to roughly estimate the field value to ionize a state. The bold solid line in Fig. 3 shows the classical ionization threshold F_c.

In the above classical picture, the Stark shift and the spatial distribution of the wavefunction are neglected. To be more precise, we take into account these factors explicitly in the following. In the parabolic coordinates, the motion in the ξ direction is bound in any value of the field. Thus for ionization to occur the electron must escape to infinity in the η direction, the potential of which direction is given by

$$V(\eta) = \frac{m^2-1}{4\eta^2} - \frac{Z_2}{\eta} - \frac{W}{2} - \frac{F}{4}\eta. \tag{26}$$

Ignoring the short range η^{-2} term, which is a good approximation for low $|m|$, the required field for ionization is given by

$$F_{Z_2} = \frac{W^2}{4Z_2}. \tag{27}$$

The separation parameter Z_2 is around $1/n$ for a blue state, $Z_2 \sim 1/2$ for a central state, and $Z_2 \sim 1$ for a red state, thus, among these states in manifold, the reddest one is most easily ionized. The ionization threshold F_{Z_2} calculated with Eq. (27) are shown by open circles in Fig. 3 (denoted F_t in the figure). This ionization process is usually called tunneling ionization.

In the field ionization of alkali Rydberg states, there occurs yet another type of ionization process called autoionization-like process[8]. This ionization is due to the coupling of the relevant state to the red continuum from the higher lying n states: This level-mixing occurs at the ionic core due to the interactions between them. This process is therefore relevant only to the non-hydrogenic atoms. With this process, the red as well as blue states, in addition to the reddest state, are also allowed to be field ionized at the lower field strength than with the tunneling process. In fact the field ionization with the autoionization-like process occurs at nearly the same field strength as the classical saddle point value. Since the occurrence of the autoionization-like process is proportional to the coupling strength to the red continuum, it decreases with increasing n, because the coupling is weakened in proportion

to n^{-4}. Also it depends on the magnetic substate m: It is dominant for low m values less than 3 due to the nature of the level mixing mentioned above[9].

3 Theory

3.1 Overview

In this section we present theoretical prescriptions to calculate the Stark energy levels and time evolution of Rydberg states related to the multilevel avoided crossing phenomena. These calculations were performed to get the theoretical predictions on the transitional behaviors at the multilevel avoided crossings and to compare them with the experimental results obtained in the present investigations.

3.2 Stark energy levels

The Hamiltonian of an alkali atom in an electric field F is given by

$$\begin{aligned} H &= \frac{1}{2m}p^2 - \frac{1}{r} + V_d + \Lambda + Fz \\ &= H_0 + Fz. \end{aligned} \tag{28}$$

These terms, V_d and Λ, are nonzero near $r = 0$. For the non-hydrogenic atom, the parabolic representation does not provide an attractive basis for the Stark problem contrary to the case of a hydrogenic atom. This is because, due to the presence of V_d and Λ, the Hamiltonian matrix in zero field is not diagonal in the parabolic basis. On the other hand, it is diagonal in the $|n\ell jm_j\rangle$ basis. For this reason we have chosen to work with the $|n\ell jm_j\rangle$ basis.

It is important to realize that the perturbative treatment of the Stark energy with the power-series expansion in a field is fundamentally inadequate because the expansion does not converge. A straightforward and effective method of calculating the energy in an electric field is the direct diagonalization of the Hamiltonian matrix. Specifically the matrix elements of H_0, including V_d and Λ, are diagonalized in the $|n\ell jm_j\rangle$ basis with quantum defect theory. The diagonal matrix elements are given by the Rydberg formula,

$$\langle n\ell jm_j|H_0|n\ell jm_j\rangle = \frac{R_{\rm alk}}{(n-\delta_{n\ell j})^2} \tag{29}$$

$$= \frac{R_{\rm alk}}{(n^*)^2}, \tag{30}$$

Table 1: ^{85}Rb quantum defect parameters [10]

Series	δ_0	δ_2	δ_4	δ_6	δ_8
$ns_{1/2}$	3.13109(2)	0.204(8)	-1.8		
$np_{1/2}$	2.65456(15)	0.388(60)	-7.904	116.437	-405.907
$np_{3/2}$	2.64145(20)	0.33(18)	-0.97495	14.6001	-44.7265
$np_{3/2,5/2}$	1.347157(80)	-0.59553(18)	-1.50517	-2.4206	19.736

where $R_{\rm alk}$ is the Rydberg constant for the alkali atom, $\delta_{n\ell j}$ is the quantum defect of an $n\ell j$ state and n^* is the effective quantum number. The value of $\delta_{n\ell j}$ is given by

$$\delta_{n\ell j} = \delta_0 + \frac{\delta_2}{(n-\delta_0)^2} + \frac{\delta_4}{(n-\delta_0)^4} + \frac{\delta_6}{(n-\delta_0)^6} + \frac{\delta_8}{(n-\delta_0)^8}\cdots, \qquad (31)$$

where δ_0, $\delta_2\ldots$ are experimentally determined parameters for the alkali atoms. The parameters δ_0, $\delta_2\ldots$ in Eq. (31) for ^{85}Rb are presented in Table 1 [10]. The virtue of the quantum defect theory is that we need not know the details of the radial dependence of V_d and Λ, which are not known exactly.

Off-diagonal matrix elements are expressed by the $|n\ell jm_j\rangle$ basis:

$$\begin{aligned}
&\langle n^*\ell jm_j|Fz|n^{*\prime}\ell' j' m_j'\rangle \\
= \;& F\delta(m_j,m_j')\delta(\ell,\ell'\pm 1)\langle n^*\ell|r|n^{*\prime}\ell\pm 1\rangle \\
&\cdot \sum_{m_\ell = m_j \pm m_s} \langle \ell, \frac{1}{2}, m_\ell, m_s|j,m_j\rangle\langle \ell', \frac{1}{2}, m_\ell, m_s|j,m_j\rangle \\
&\cdot\langle \ell, m_\ell|\hat{z}|\ell\pm 1, m_\ell\rangle, \qquad (32)
\end{aligned}$$

where the first two factors in the sum are Clebsch-Gordan coefficients and $\hat{z} = z/|z|$. The angular part of the matrix elements are derived by using algebra of spherical harmonics,

$$\begin{aligned}
\langle \ell, m_\ell|\hat{z}|\ell-1, m_\ell\rangle &= \sqrt{\frac{\ell^2-m_\ell^2}{(2\ell+1)(2\ell-1)}}, \\
\langle \ell, m_\ell|\hat{z}|\ell+1, m_\ell\rangle &= \sqrt{\frac{(\ell+1)^2-m_\ell^2}{(2\ell+3)(2\ell+1)}}. \qquad (33)
\end{aligned}$$

The radial dipole matrix elements are calculated under the Coulomb approximation following the method by Davydkin and Zon [11],

$$\langle n^*\ell|r|n'^*\ell\pm 1\rangle$$

$$= \frac{\bar{n}^*}{\Delta Z}\left\{\frac{\sin\pi\Delta}{\pi\Delta}\left[\Delta(1-\varepsilon) \mp \frac{\sqrt{1-\varepsilon^2}}{\varepsilon}\right]\right\}$$
$$+\frac{\bar{n}^*}{\Delta Z}\left\{\frac{d}{dx}J_\Delta(-x) \pm \frac{\sqrt{1-\varepsilon^2}}{\varepsilon}J_\Delta(-x)\right\}, \quad (34)$$

$$\bar{n}^* = \sqrt{n^* n^{*\prime}}, \quad (35)$$
$$\bar{\ell} = \frac{\ell+\ell'}{2}, \quad (36)$$
$$\varepsilon = \sqrt{1-\frac{(\bar{\ell}+1/2)^2}{(\bar{n}^*)^2}}, \quad (37)$$
$$\Delta = n^{*\prime} - n^*, \quad (38)$$
$$x = \varepsilon\Delta, \quad (39)$$
$$J_\Delta(S) = \frac{1}{\pi}\int_0^\pi \cos(\Delta\theta - S\sin\theta)d\theta. \quad (40)$$

Equation (34) is an analytic expression for the dipole matrix elements corresponding to transitions between Rydberg states with $|\Delta| \ll n^*, n^{*\prime}$. We note here that the approximation used in Eq. (34) is more accurate when n^* becomes larger and thus it gives quite satisfactory results for the Rydberg states with $n > 100$. Accuracy of the calculation of the radial matrix elements was discussed by Kishimoto[12]

With these matrix elements diagonalization of the Hamiltonian matrix is performed to obtain the eigenvalues and eigenstates in each electric field. The Stark map shown in Fig.4 is an example of the calculated energy level structure of the Rydberg states of ^{85}Rb around $n = 110$ manifold with $|m_j| = 1/2$. In this calculation, the terms included in the basis set of the diagonalization are $105 \leq n \leq 115$ for each $|m_j|$. This basis set is adequate within the calculated range of the field, up to 0.3 V/cm. A critical discussion on this truncation effect and others was given in [12].

3.3 Two-level avoided crossing

A computational method to calculate the transition probabilities at the multilevel avoided crossings was developed[12], in which the actual pulse profile with any shape can be precisely taken into account during an arbitrary time duration.

To study the adiabatic and non-adiabatic transitions, we first consider the simple case where only two levels cross and the time dependence of their energy levels are arbitrary functions of time t. This simple case was studied by Rubmmark *et al.* [6]. We consider a two-level system governed by a

Hamiltonian H_0 which depends explicitly on t. We denote the eigenvalues of H_0 by $\Omega_1(t)$ and $\Omega_2(t)$ and the eigenstates by $|1\rangle$ and $|2\rangle$. The eigenstates are assumed to be independent of t. Next we consider the effect of a perturbation V, which breaks the symmetry of H_0 and has no dependence on t. The Hamiltonian in this case is given in the $\{|1\rangle, |2\rangle\}$ basis

$$H = \begin{pmatrix} \omega_1(t) & \frac{1}{2}|\omega_0|e^{-i\theta} \\ \frac{1}{2}|\omega_0|e^{+i\theta} & \omega_2(t) \end{pmatrix}, \tag{41}$$

where ω_0, $\omega_1(t)$ and $\omega_2(t)$ are written by,

$$\begin{aligned} \frac{1}{2}|\omega_0|e^{-i\theta} &= \langle 1|V|2\rangle, \\ \omega_1(t) &= \Omega_1(t) + \langle 1|V|1\rangle, \\ \omega_2(t) &= \Omega_2(t) + \langle 2|V|2\rangle. \end{aligned} \tag{42}$$

The separation at the center of the avoided crossing is $|\omega_0|$. The time dependent Shrödinger equation,

$$i\frac{d}{dt}|\Psi(t)\rangle = H|\Psi(t)\rangle \tag{43}$$

is then solved by taking,

$$|\Psi(t)\rangle = C_1(t)\exp\left(-i\int_{t_i}^{t} dt'\omega_1(t')\right)|1\rangle + C_2(t)\exp\left(-i\int_{t_i}^{t} dt'\omega_2(t')\right)|2\rangle. \tag{44}$$

Substituting Eq. (44) into Eq. (43) results in

$$i\dot{C}_1(t) = \frac{\omega_0}{2}e^{-i\theta}\exp\left(i\int_{t_i}^{t} dt'(\omega_1(t') - \omega_2(t')\right)C_2(t), \tag{45}$$

$$i\dot{C}_2(t) = \frac{\omega_0}{2}e^{+i\theta}\exp\left(i\int_{t_i}^{t} dt'(\omega_2(t') - \omega_1(t')\right)C_1(t). \tag{46}$$

At the initial time $t = t_i$, the system is assumed to be in the upper eigenstate,

$$|b_i\rangle = \beta_{1i}|1\rangle + \beta_{2i}|2\rangle, \tag{47}$$

where β_{1i} and β_{2i} are determined from the initial condition at $t = t_i$ and $\beta_{1i} = C_1(t_i)$ and $\beta_{2i} = C_2(t_i)$. We are interested in the probability that the final state is in the lower eigenstate $|a_f\rangle$ at $t = t_f$,

$$|a_f\rangle = \alpha_{1f}|1\rangle + \alpha_{2f}|2\rangle. \tag{48}$$

The transition probability is explicitly given by

$$P = |\langle a_f|\Psi(t_f)\rangle|^2 \tag{49}$$

$$= |\alpha_{1f}^* C_1(t_f) + \alpha_{2f}^* C_2(t_f)|^2. \tag{50}$$

3.4 Multilevel avoided crossings

The above formalism is extended to the case with many number of relevant energy states in a time varying electric field. Under a pulsed electric field, the Hamiltonian is given by

$$\begin{aligned} H &= \frac{1}{2m}p^2 - 1/r + V_d + \Lambda + F_x(t)x + F_y(t)y + F_z(t)z \\ &= H_0 + F_x(t)x + F_y(t)y + F_z(t)z. \end{aligned} \tag{51}$$

The matrix elements of x and y are calculated as follows.

$$\begin{aligned} & \langle n,\ell,m_\ell|x+iy|n',\ell+1,m_\ell+1\rangle \\ =\ & \langle n,\ell,m_\ell|\hat{x}+i\hat{y}|n',\ell+1,m_\ell+1\rangle\langle n,\ell|r|n',\ell+1\rangle \\ =\ & +\sqrt{\frac{(\ell+m_\ell+2)(\ell+m_\ell+1)}{(2\ell+3)(2\ell+1)}}\langle n,\ell|r|n',\ell+1\rangle, \end{aligned} \tag{52}$$

$$\begin{aligned} & \langle n,\ell,m_\ell|x-iy|n',\ell+1,m_\ell-1\rangle \\ =\ & -\sqrt{\frac{(\ell-m_\ell+2)(\ell-m_\ell+1)}{(2\ell+3)(2\ell+1)}}\langle n,\ell|r|n',\ell+1\rangle, \end{aligned} \tag{53}$$

$$\begin{aligned} & \langle n,\ell,m_\ell|x+iy|n',\ell-1,m_\ell+1\rangle \\ =\ & -\sqrt{\frac{(\ell-m_\ell)(\ell-m_\ell-1)}{(2\ell+1)(2\ell-1)}}\langle n,\ell|r|n',\ell-1\rangle, \end{aligned} \tag{54}$$

$$\begin{aligned} & \langle n,l,m_\ell|x-iy|n',\ell-1,m_\ell-1\rangle \\ =\ & -\sqrt{\frac{(\ell+m_\ell)(\ell+m_\ell-1)}{(2\ell+1)(2\ell-1)}}\langle n,\ell|r|n',\ell-1\rangle. \end{aligned} \tag{55}$$

With these matrix elements, the matrix element $\langle n^*\ell j m_j|F_q q|n^{*\prime}\ell' j' m_j'\rangle$ is expressed as

$$\begin{aligned} & \langle n^*\ell j m_j|F_q q|n^{*\prime}\ell' j' m_j'\rangle \\ =\ & F_q\delta(m_j,m_j')\delta(\ell,\ell'\pm1)\langle n^*\ell|r|n^{*\prime}\ell'\pm1\rangle \\ & \cdot\sum_{m_\ell=m_j\pm m_s}\langle\ell,\frac{1}{2},m_\ell,m_s|j,m_j\rangle\langle\ell',\frac{1}{2},m_\ell,m_s|j,m_j\rangle\langle\ell m_\ell|\hat{q}|\ell' m_\ell\rangle, \end{aligned} \tag{56}$$

where $q = x, y, z$ and $\hat{q} = q/|q|$.

We write the initial state as $|n, Z_1, m_j; (F_i)\rangle$ and the final eigenstate as $|\widetilde{n}, \widetilde{Z}_1, \widetilde{m}_j; (F_f)\rangle$. These eigenstates are obtained by the diagonalization of the Hamiltonian matrix at $t = t_i$ and t_f, respectively,

$$|n, Z_1, m_j; (F_i)\rangle = \sum_{n,j,m_j} u_{n,\ell,j,m_j}^{n,Z_1,m_j}(F_i)|n,\ell,j,m_j\rangle, \tag{57}$$

$$|\widetilde{n},\widetilde{Z}_1,\widetilde{m}_j;(F_f)\rangle = \sum_{n,j,m_j} u^{\widetilde{n},\widetilde{Z}_1,\widetilde{m}_j}_{n,\ell,j,m_j}(F_f)|n,\ell,j,m_j\rangle. \quad (58)$$

We use the eigenstates $|n,Z_1,m_j;(F_i)\rangle$ as the basis set. The Hamiltonian is diagonalized at $t=t_i$ at the field $F=(0,0,F_z(t_i))$,

$$\begin{aligned}&\langle n',Z_1',m_j';(F_i)|H(t_i)|n,Z_1,m_j;(F_i)\rangle\\ =\;& W_{n,Z_1,m_j}\delta(n,n')\delta(Z_1,Z_1')\delta(m_j,m_j'). \end{aligned}\quad (59)$$

At time t in the field $F(t)=(F_x(t),F_y(t),F_z(t))$, the Hamiltonian matrix elements are given by

$$\begin{aligned}&\langle n',Z_1',m_j';(F_i)|H(t)|n,Z_1,m_j;(F_i)\rangle\\ =\;& W_{n,Z_1,m_j}(F_i)\delta(n,n')\delta(Z_1,Z_1')\delta(m_j,m_j')\\ &+\sum_{q=x,y,z}\Delta F_q(t)\langle n',Z_1',m_j';(F_i)|q|n,Z_1,m_j;(F_i)\rangle, \end{aligned}\quad (60)$$

where $\Delta F_q(t)$ is given by

$$\Delta F_q(t) = F_q(t)-F_q(t_i), \quad (61)$$

and $\langle n',Z_1',m_j';(F_i)|q|n,Z_1,m_j;(F_i)\rangle$ for $q=x,y,z$ is given by

$$\begin{aligned}\langle n',Z_1',m_j';(F_i)|q|n,Z_1,m_j;(F_i)\rangle =\;& \sum_{n,\ell,j,m_j}\sum_{n',\ell',j',m_j'} u^{n',Z_1',m_j'}_{n',\ell',j',m_j'}(F_i)^* u^{n,Z_1,m_j}_{n,\ell,j,m_j}(F_i)\\ &\cdot\langle n',\ell',j',m_j'|q|n,\ell,j,m_j\rangle. \end{aligned}\quad (62)$$

We then solve the Shrödinger equation,

$$i\frac{d}{dt}|\Psi(t)\rangle = H(t)|\Psi(t)\rangle, \quad (63)$$

$$|\Psi(t)\rangle = \sum_{n',Z_1',m_j'} C_{n',Z_1',m_j'}(t)\exp(-i\phi_{n',Z_1',m_j'}(t))|n',Z_1',m_j'\rangle, \quad (64)$$

$$\begin{aligned}\phi_{n,Z_1,m_j}(t) =\;& \int_{t_i}^{t} dt' W_{n,Z_1,m_j}(F_i)\\ &+\sum_{q=x,y,z}\int_{t_i}^{t} dt'\Delta F_q(t')\langle n,Z_1,m_j|q|n,Z_1,m_j\rangle, \end{aligned}\quad (65)$$

$$\begin{aligned}i\dot{C}_{n,Z_1,m_j}(t) =\;& \sum_{n',Z_1',m_j'\neq n,Z_1,m_j} C_{n',Z_1',m_j'}(t)\exp\{i(\phi_{n,Z_1,m_j}(t)-\phi_{n',Z_1',m_j'}(t))\}\\ &\cdot\sum_{q=x,y,z}\Delta F_q(t)\langle n,Z_1,m_j|q|n',Z_1',m_j'\rangle. \end{aligned}\quad (66)$$

The transition probability from an eigenstate $|n, Z_1, m_j; (F_f)\rangle$ at $t = t_i$ to an eigenstate $|\widetilde{n}, \widetilde{Z}_1, \widetilde{m}_j; (F_f)\rangle$ at $t = t_f$ is obtained in the $|n\ell j m_j\rangle$ basis,

$$P_{\widetilde{n},\widetilde{Z}_1,\widetilde{m}_j} = |\langle \widetilde{n}, \widetilde{Z}_1, \widetilde{m}_j | \Psi(t_f)\rangle|^2 \tag{67}$$

$$= \Big| \sum_{n',\ell',j',m'_j} \sum_{n,Z_1,m_j} u^{\widetilde{n},\widetilde{Z}_1,\widetilde{m}_j}_{n',\ell',j',m'_j}(F_f)^* u^{n,Z_1,m_j}_{n',\ell',j',m'_j}(F_i) \cdot C_{n,Z_1,m_j}(t_f) \exp(-i\phi_{n,Z_1,m_j}(t_f)) \Big|^2. \tag{68}$$

3.5 Time evolution in a rotating electric field

In the present experiment, special care was taken to reduce the stray electric field and to precisely control the transverse electric field during the field ionization process. This is due to the strong effect of the rotating electric field on the field ionization process as investigated in detail by Yamada[9].

The effect of a rotating electric field on the Rydberg atoms was previously investigated by a number of authors[13, 14, 15, 16, 17, 18] in relation to produce and preserve the circular states in the environment of external electromagnetic field perturbations. Present study with a rotating electric field has different aspect from these previous investigations in the sense that we are mainly focussed on its effect on the field ionization process and our theoretical treatment on this effect is rather based on the theoretical development of Yamada[9]. Our main aim to apply the transverse electric field is thus to clearly observe the transitional behavior with the signals from the tunneling ionization processes.

4 Experimental setup and procedure

4.1 Setup

In this section, experimental apparatus, setup and procedure in the present study are described. The overall setup in the present experiment is schematically shown in Fig. 5. Thermal atomic beam of Rb is introduced into the laser interaction area which is included in the field ionization electrodes. The electrons liberated from the field ionization are guided to a channel electron multiplier through two sheets of grid mesh placed on one electrode plate. The whole system is placed in a vacuum chamber. Special care was taken to reduce the stray electric field in the laser interaction and field ionization regions as described later in detail.

The pulsed field ionization electrodes consist of two parallel plates of 200 mm length and 200 mm width. The distance between the electrodes is

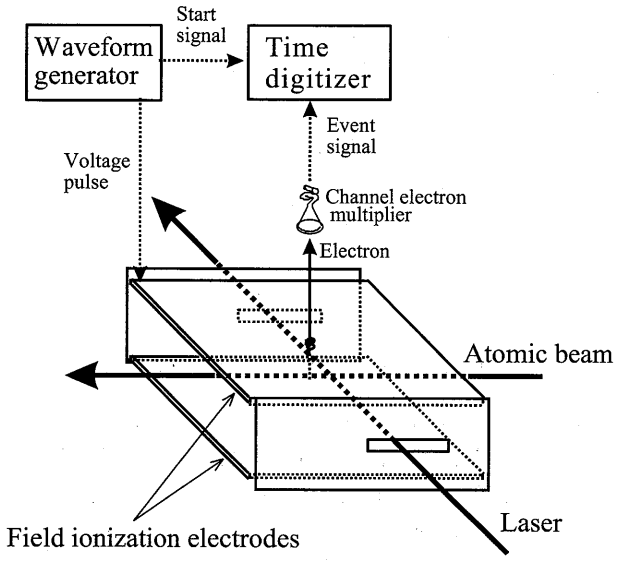

Figure 5: Schematic view of the setup of the present experiment. The field ionization pulse is applied to the electrodes parallel to the laser and atomic beams, while a transverse electric field is applied to the electrodes perpendicular to the laser beam.

60 mm. Two sheets of fine copper grid mesh are incorporated into the area of $5\times$ 5 mm^2 in one of the electrode plates to pass through and detect the electrons. The diameter of the mesh wire was 0.1 mm so that the transmission through the two mesh becomes 90%. Another pair of copper plates were also installed into the area which is set perpendicular to the field ionization electrodes. This plates are used to apply the transverse electric field during the field ionization.

4.2 Pulsed field ionization

The pulse voltage applied to the SFI electrodes is shown in Fig. 6. The voltage rises slowly from the offset value v_o to v_s during t_s, and then rises abruptly to v_f during t_f. We call these components "slow" and "fast' component, respectively. The peak field is kept for a time t_h, "holding time", then the voltage goes down to the offset value v_o. The Rydberg atoms are initially excited in a field produced by the applied offset voltage v_o. The voltage v_o is also used to compensate the stray field. The Rydberg atoms are mainly ionized at the fast component during t_f, but a state with a longer lifetime

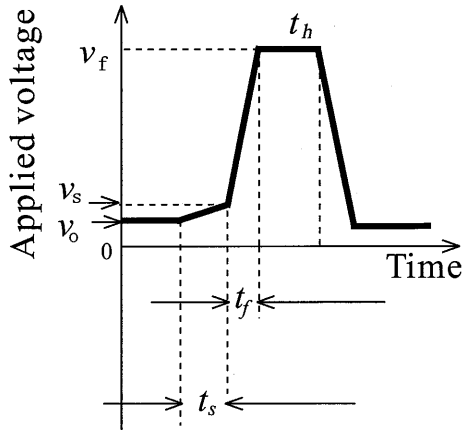

Figure 6: Pulse shape applied to the electrodes for the field ionization. The fast component $(v_s - v_f)$ is used to field ionize the Rydberg states with a high slew rate regime, while the slow component $(v_o - v_s)$ is used to drive the excited $113s_{1/2}$ Stark state to a particular field value F_r adiabatically or non-adiabatically. The slew rates of the fast $(v_s - v_f)$ and slow $(v_o - v_s)$ components are varied independently.

than t_f has some probability to be ionized during the holding time t_h.

The applied electric field strength is given by

$$F_f = v_f/l, \tag{69}$$

where l (60 mm) is the distance between the electrodes. Then the slew rate S_f is given by

$$S_f = F_f/t_f. \tag{70}$$

The pulse sequence is produced with a waveform generator AWG420 (Sony-Tektronix) and amplified by fast amplifiers. It is possible to vary the slew rates of the fast and slow components independently and to set the offset voltage v_o and the slow component v_s to be positive or negative. The slew rate of the fast component is varied to see the effect of a pulsed field shape on the field ionization characteristics, while that of the slow component is used to drive the excited Stark state to a particular field value adiabatically or non-adiabatically. The slew rate can be increased up to 50 V/(cmμs). The offset voltage is applied to vary the static field at the excitation region of the Rydberg states.

4.3 Optics and laser system

Two step excitation was adapted to excite ^{85}Rb atoms from the $5s_{1/2}$ ground state to the Rydberg $n\ell j$ state through the second excited state $5p_{3/2}$, as shown in Fig. 7.

A diode laser of Sharp GH0780MA2C (780 nm) was used for the first step excitation. The temperature(+10 °C) and the current(135 mA) were controlled to stabilize the wavelength. The power of the diode laser was 30 mW at 780 nm. and the line widths of the diode laser was $\sim$ 30 MHz.

A dye laser of Coherent 899-29 of coumarin 102 excited by a Kr ion laser was used for the second step excitation. The line width of the dye laser was $\sim$ 500 kHz and the power of the dye laser was 200 mW at 479 nm with 3 W excitation power of the Kr ion laser.

The optical setup is shown in Fig. 8. Two laser beams were mixed by a beam-splitter outside the experimental chamber.

The following technique was used to lock the wavelength of the diode laser to the first step excitation wavelength, as shown in Fig. 9.

A small fraction of the laser beam from the beam sampler passed through the $\lambda/4$ plate and were injected perpendicularly (*i.e.* Doppler free) into a thermal atomic beam of Rb installed separately in a fluorescence detection chamber. The ground state atoms were excited to the $5p_{3/2}$ state and the fluorescence emitted during the deexcitation process to the ground state was detected with a photomultiplier and this signal was used to control the diode current. The transition used here was the transition between $5s_{1/2}\,(F = 3)$ and $5p_{3/2}\,(F = 4)$ of ^{85}Rb$\,(I = 5/2)$. Since the oscillator strength of this transition is the strongest and the excited $F = 4$ state always deexcites to the ground state of $F = 3$ without the optical pumping effect, the intensity of the fluorescence is also the strongest.

At the laser excitation point, an oscillating magnetic field ($\sim$ 10 G) was applied parallel to the laser beam in order to obtain a phase-sensitive fluorescence signals. The laser beam was circularly polarized with the $\lambda/4$ plate. Due to the Zeeman effect with the oscillating magnetic field, the transition frequency and the fluorescence signals were also modulated at the frequency of the solenoid current. The modulated fluorescence signal and the solenoid current were fed into a lock-in-amplifier as an input signal and a reference signal, respectively. The output of the lock-in-amplifier was fed to the current controller for the diode laser as a negative feedback signal so as to lock the wavelength of the diode laser to that of the transition between $5s_{1/2}\,(F = 3)$ and $5p_{3/2}\,(F = 4)$. The oscillating magnetic field was generated by a solenoid coil in which a sine-wave current of 50 $\sim$ 100 Hz was applied.

The wavelength of the ring dye laser was stable enough to be used for

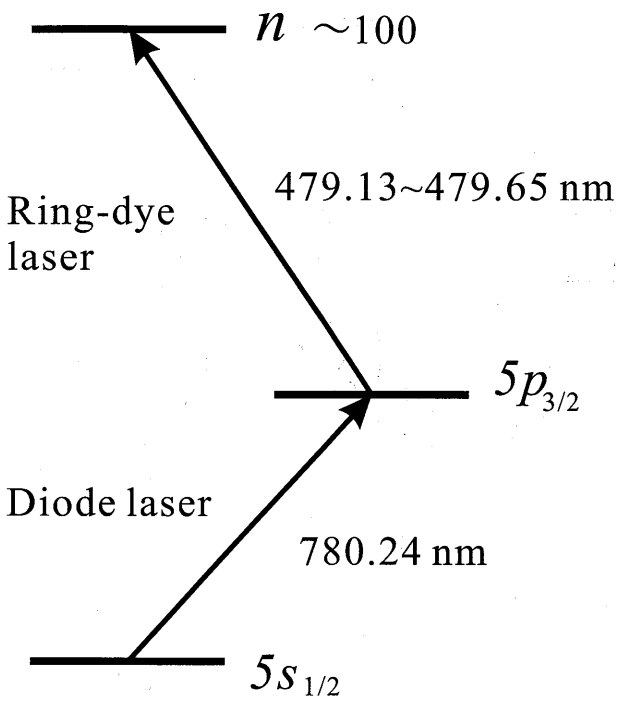

Figure 7: Two-step laser excitation scheme adopted for populating the initial Rydberg states.

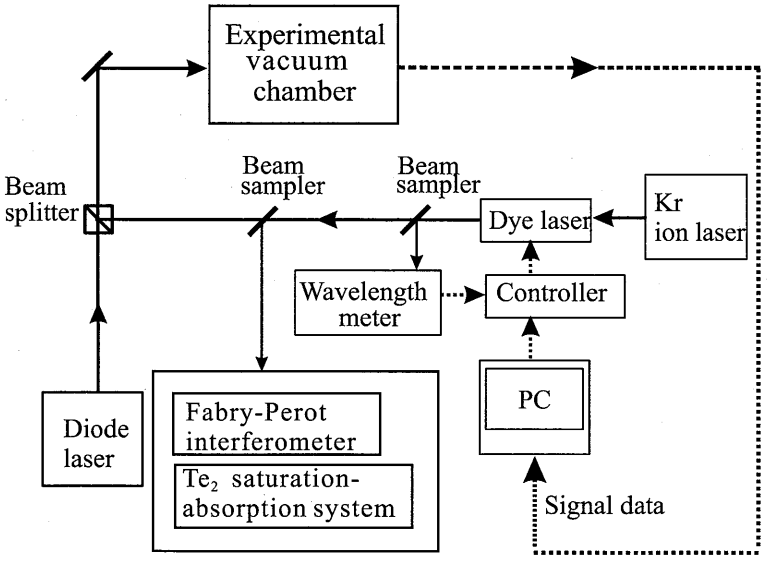

Figure 8: Schematic diagram of the present optical setup.

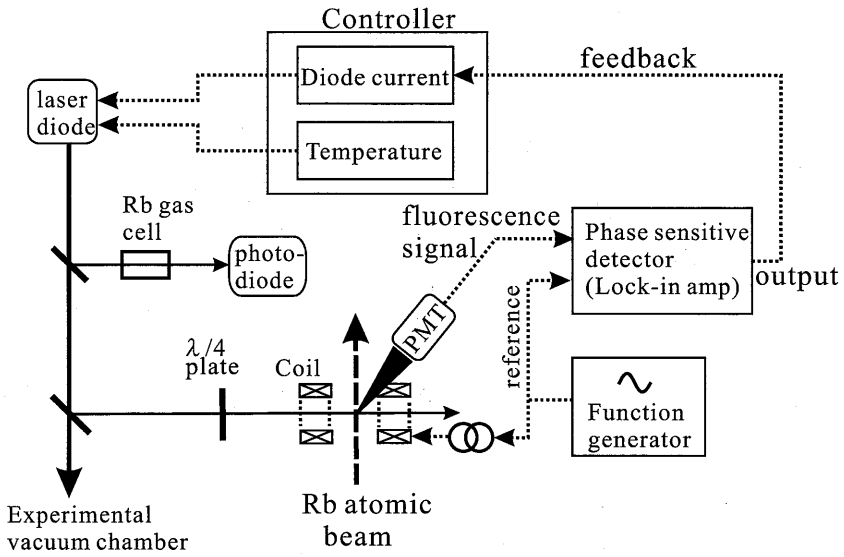

Figure 9: Schematic diagram of the wavelength control system for the first diode laser. Fluorescence signals from the excited $5p_{3/2}$ state to the ground state of ^{85}Rm atoms are used to control the current of the laser diode, thereby locking the wavelength of the laser to the corresponding excitation resonance. The Rb oven for this purpose was separately installed from the main experimental sysytem.

our experiment for more than several minutes without any external control in its original performance. In order to obtain still longer stability further, the dye laser was controlled with the ionization signal counts of the excited Rydberg states, as described in more detail in the next section.

In the present experiment, it is essential to precisely measure the electric field at the laser interaction and field ionization regions. Specifically the transverse as well as longitudinal electric fields were accurately determined before performing the measurements. For this purpose, we installed a Fabry-Perot interferometer with FSR of 150 MHz and a saturation-absorption detection system with Te_2 cell: With these system more precise wavelength of the excitation laser can be obtained from the frequency scanning of the second laser. These installed system is schematically shown in Fig.10. Accurate determination of the elelctric field was performed with the aid of the semiemplical formula of the second- and fourth- order Stark shifts obtained by our previous work[7].

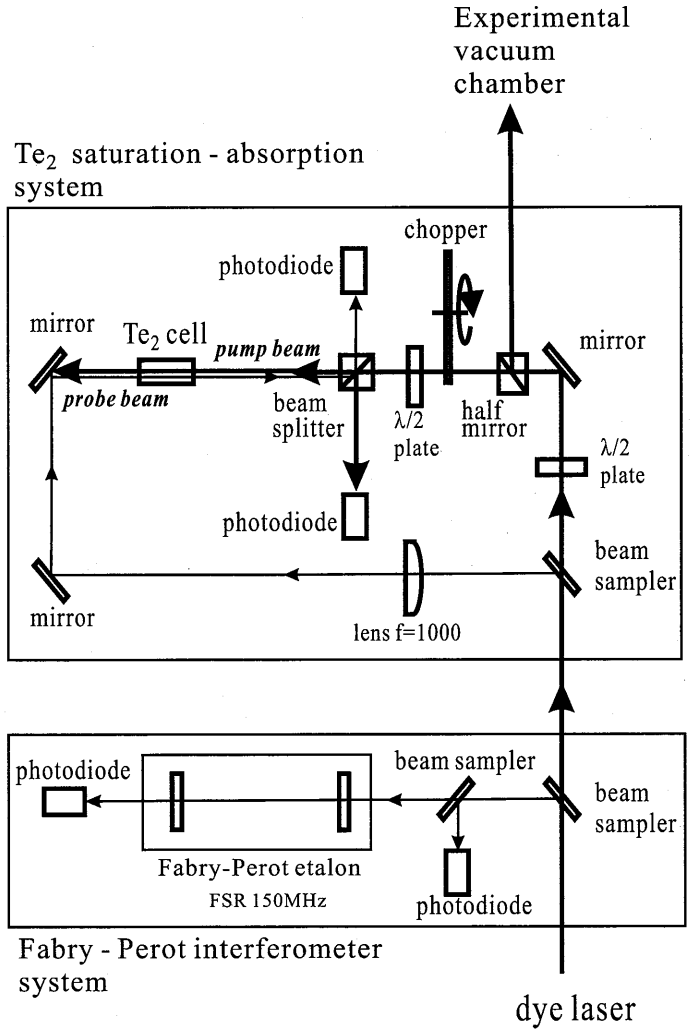

Figure 10: Schematic diagram of the wavelength calibration system for the second ring-dye laser. Saturation-absorption signals from the Te_2 and the signals from a Fabry-Perot interferometer with 150 MHz FSR are used to precisely determine the wavelength of the second laser. This calibration system is operated at the same time with the experiments.

4.4 Data aquisition and processing

The electron signals from the channel electron multiplier were amplified by a pre-amplifier A250 (Amptek) and a main amplifier AN302/NL (ORTEC) and then fed to a discriminator KN241 (Kaizu). The field ionization signals were then amplified and fed to a time digitizer p7886 (Fast ComTek) after the pulse hight discrimination. The signal acquisition gate of the digitizer was synchronized with the applied field ionization pulse, thus the timing information can be transformed to field ionization spectra. The data were analyzed on-line with the LabVIEW data acquisition system on a computer. The whole data were analyzed off-line as well as on-line with LabVIEW programs.

Long term locking of the wavelength of the second laser was carried out with the following procedure.

1)initial setting: The dye laser frequency is set to near the transition of interest, for example, to the $5p_{3/2}$-110 manifold transition with the internal wavelength meter and the controller of the dye laser.

2)laser frequency scanning: The laser frequency is scanned externally by driving the scan-control voltage from a computer. The step size of the scanning is $1 \sim 5$ MHz. During the scanning, the field ionization voltage v_f is kept constant and the ionization signals are counted.

3)peak holding: When the peak of the signal for the state of interest is observed, then the scan-control voltage is fixed at the peak position.

4)data taking: various data taking is performed according to the experimental detail.

5) re-scanning and peak holding: The laser frequency is scanned again. The frequency scanning is carried out in a narrow range around the previous setup frequency. The scan-control voltage is set again to make the signals maximum. This procedure is automatically repeated for some cycles. All these processes are controlled by a LabVIEW program system.

5 Results and discussion

5.1 Experimental results

5.1.1 Effect of a rotating electric field and field ionization spectra

In Fig.11 shown is typical excitation spectrum of the Rb Rydberg states around n=110 manifold. Here the static electric field of 33 mV/cm was applied at the laser interaction region so that the p state as well as splitting manifold states are seen to be excited together with the allowed states at

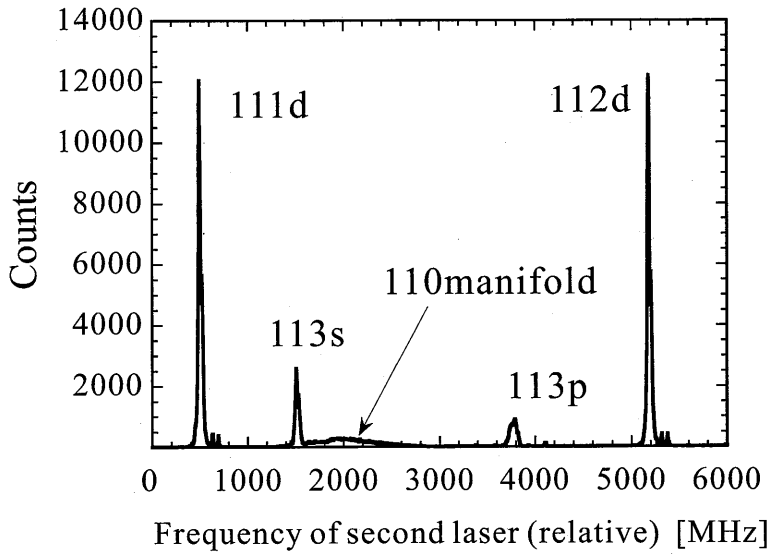

Figure 11: Typical excitation spectrum of the Rb Rydberg states around n=110 manifold. Here the static electric field of 33 mV/cm was applied at the laser interaction region.

zero-electric field.

By locking the second laser wavelength at the excited s state peak, we firstly examined the effect of a rotating electric field on the field ionization processes. To do this accurately, we need to know exactly the stray electric field at the field ionization region. Especially important here is the transverse stray electric field, because the transverse component is added to the externally applied transverse field, thus bringing some ambiguity to the effect of the transverse field. Note that the longitudinal stray field with the externally applied field does not much affect the final results, since the stray field just shifts the externally applied field value relative in time and brings negligible contributions to the finally reached higher electric field.

For this purpose, we do the following procedure to determine the stray electric field at the region of grid mesh where the atoms are ionized and detected. Firstly the higher excited Rydberg states, for example the states around n=130 manifold, are excited at the grid mesh region by applying statically various external field along the direction of the field ionization pulse, and the resulting electric field is determined from the Stark shifts of the s, p and d states as described in somewhat detail in [7]. Then these data on the electric field are plotted as a function of the externally applied electric

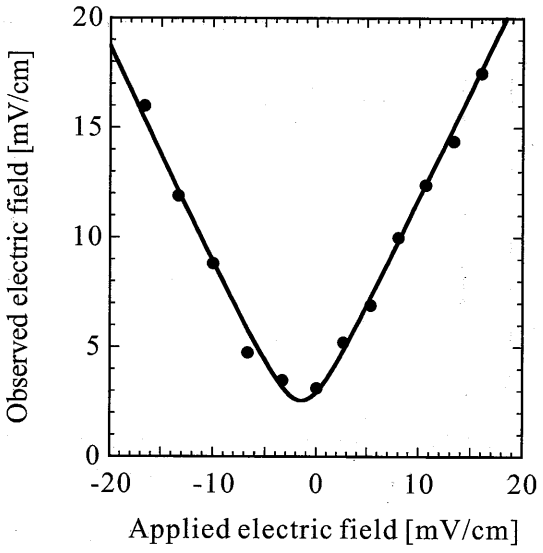

Figure 12: Determination of the stray electric field at the grid mesh region of field ionization electrodes: The electric field is measured by varying the externally applied electric field with use of the known Stark shifts of the highly excited s, p and d states around n=130. The stray electric field in the longitudinal as well as transverse directions are then determined by fitting the observed data with the known dependence on these values.

field. In Fig.12 shown is an example of such data obtained to determine the stray field in the ionization region:

From this data of the observed field F_{obs}, the longitudinal and transverse electric fields are determined by fitting the data with a function given by

$$F_{obs} = \left((F_{app} + F_{long})^2 + F_{trans}^2\right)^{1/2}, \tag{71}$$

where F_{app}, F_{long}, and F_{trans} are the externally applied electric field, longitudinal and transverse components of the stray field, respectively. In the above case shown in Fig.12, the stray electric field was determined to be F_{long}=1.5 mV/cm, and F_{trans}= 2.5 mV/cm, respectively. The position dependence of the stray electric field was measured by varying the laser excitation positions with the procedure above. Variation of the stray electric field was found to be smaller than 0.5 mV/cm over the whole region of the field ionization.

As clarified and described in detail by Yamada [9], the effect of a rotating electric field on the field ionization processes is profound for the splitting manifold states: This is mainly due to the rotation of the angular momen-

tum which partially follow the rotation of the electric field (intermediate between the adiabatic and diabatic passages). In the case of $s_{1/2}$ state, similar effect of a rotating electric field was observed also in the present case of $113s_{1/2}$ state : In Fig.13 shown are the spectra resulting from the effect of the transverse electric field F_{trans}. With increasing F_{trans} the fraction of the tunneling ionization component increases profoundly and the peak due to the autoionization-like process disappears almost completely at higher transverse field. The fraction of the tunneling process is plotted in Fig.14 as a function of the applied transverse electric field. This result indicates that the spin direction of the initially populated $s_{1/2}$ state with $|m_j|$=1/2 is rotated with the applied electric field, and some component of the higher magnetic substates are populated. Since the tunneling process is more enhanced with higher m states (mostly $m \geq 3$), the fraction of the tunneling component increases with increasing transverse field.

From the above experimental results on the effect of a rotating electric field, the following measurements on the multilevel avoided crossings were performed with an applied transverse elelctric field to enhance the component of the tunneling field ionization process. Typical field ionization spectrum is shown in Fig.15 where the transverse electric field of 20 mV/cm was applied at the field ionization region. Here the $113s_{1/2}$ state was initially excited at the electric field of 24 mV/cm, well isolated position from the adjacent manifold state, and then was driven to the field of 44 mV/cm with a slew rate of 42 mV/(cm μs). The state was then driven to higher electric field with high slew rate regime to be finally field ionized. The lowest peak observed is due to the autoionization-like process, and higher two peaks correspond to the components from the tunneling process as seen from the comparison with the paths drawn in the relevant Stark map shown at the upper part of the figure. Occurrence of the two processes in the field ionization spectra is the common phenomena for these highly excited Rydberg states as revealed in our previous experiments[8, 19]. To be noted here, two peaks from the tunneling process indicate two different paths in the Stark map, diabatic and adiabatic paths, respectively, as shown in the figure.

5.1.2 Transitions at multilevel avoided crossings

Based on the above ionization feature, the transitional behavior of the $113s_{1/2}$ state from the isolated Stark position to the point of field F_r was investigated with various slew rates. In Fig.16 shown are some of the spectra of the field ionization measured at various slew rates. The value of F_r in this measurement was 40 mV/cm. With increasing slew rate, the tunneling ionization peak with the adiabatic path (path to TU_a in Fig.15) decreases,

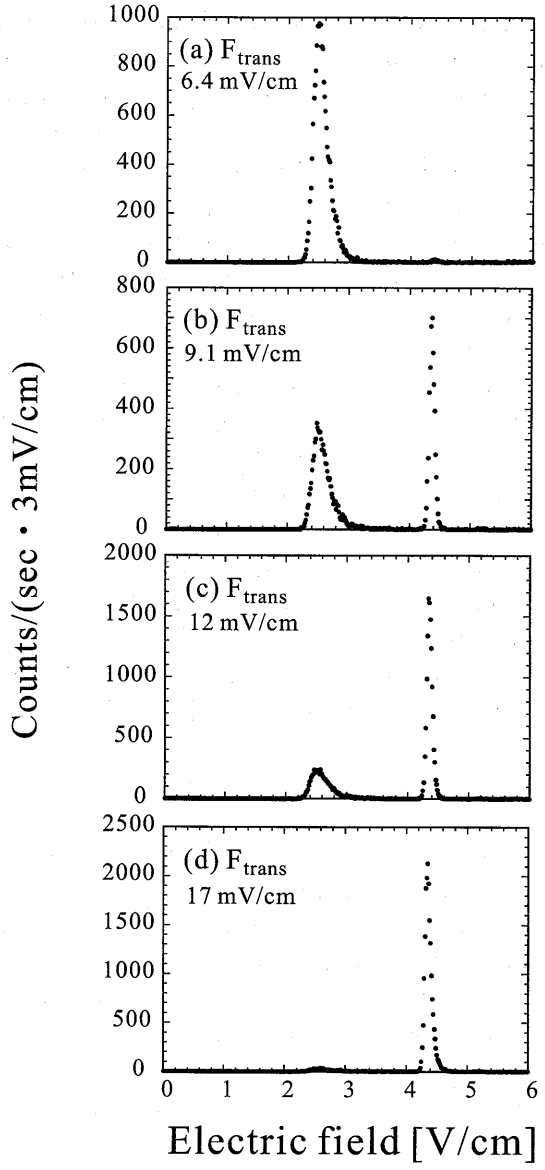

Figure 13: Some of the observed field ionization spectra with varying transverse electric field F_{trans}. The longitudinal electric field was applied from zero to a high field for the field ionization. With increasing transverse field, the ionization signals from the autoionization-like process (lower peak) decreases, while that from the tunneling ionization process (upper peak) increases. This observation clearly shows the effect of the rotating electric field on the field ionization processes.

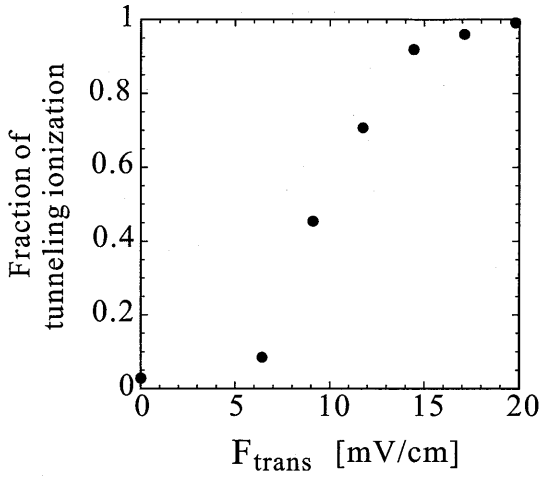

Figure 14: Fraction of ionization signals $113s_{1/2}$ state from the tunneling ionization process to the total ionization signals as a function of the applied transverse electric field. With zero transverse field, almost no tunneling ionization occurs, while at 20 mV/cm transverse field, the tunneling ionization signals dominates and almost saturates.

while the peak due to the diabatic path (path to TU_d in Fig.15) increases. This feature indicates clearly that with increasing slew rate, the transition probability to the diabatic path increases.

Fig.17 shows the slew rate dependence of the above transition probabilities with various values of F_r. Here the ordinate represents the ratio of the adiabatic to diabatic tunneling components. It is clearly seen that the slew rate dependence of the transition probability changes profoundly with the value of F_r.

It is noted here that the value of F_r, the electric field strength to which the state is driven with slow component (v_s in Fig.6), should be carefully determined experimentally. Since the state merges into the n=110 manifold at this field, we determined the value with the following procedure: By applying the electric field F_r statically, we first measure the laser excitation spectrum of higher manifold state as shown, as an example, in Fig.18. From this spectrum, we determine the energy difference between the $s_{1/2}$ state and the p and d states. This difference is then compared with theoretical predictions from the Hamiltonian diagonalization procedure. The Stark energy levels are calculated with the Hamiltonian diagonalization procedure as described in section3.2 up to the field value over F_r. Typical Stark energy map

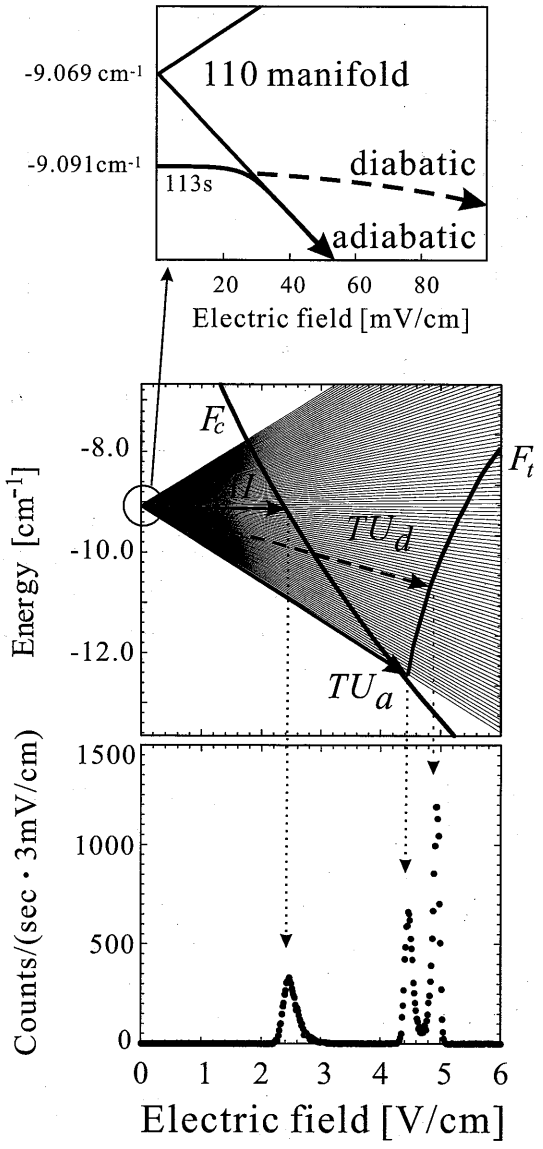

Figure 15: Typical field ionization spectrum of $113s_{1/2}$ state with its relevant Stark energy diagram. Driving the $s_{1/2}$ state into an electric field over the first avoided crossing point, three peaks appears in the field ionization spectrum:One is from the autoionization-like process (lowest peak) with the path AI, and the others are from the tunneling ionization processes with adiabatic path (middle peak) of TU_a and diabatic path (upper peak) of TU_d, respectively.

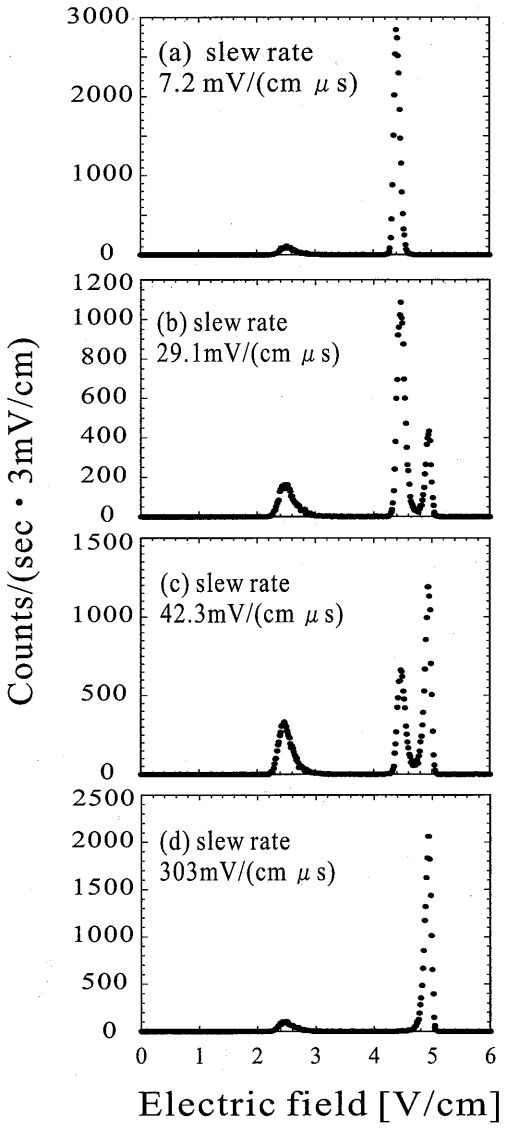

Figure 16: Some of the field ionization spectra of $113s_{1/2}$ state with varying slew rate in the slow component of the applied pulse. With increasing slew rate, the tunneling-ionization peak (middle) corresponding to the adiabatic path transferring the s state to reddest manifold state decreases, while the peak (upper) to the diabatic path increases. Here the s state was initially populated at the electric field strength of 20 mV/cm and driven into the manifold-merged region at 33 mV/cm electric field F_r. Applied transverse electric field F_{trans} is 20 mV/cm.

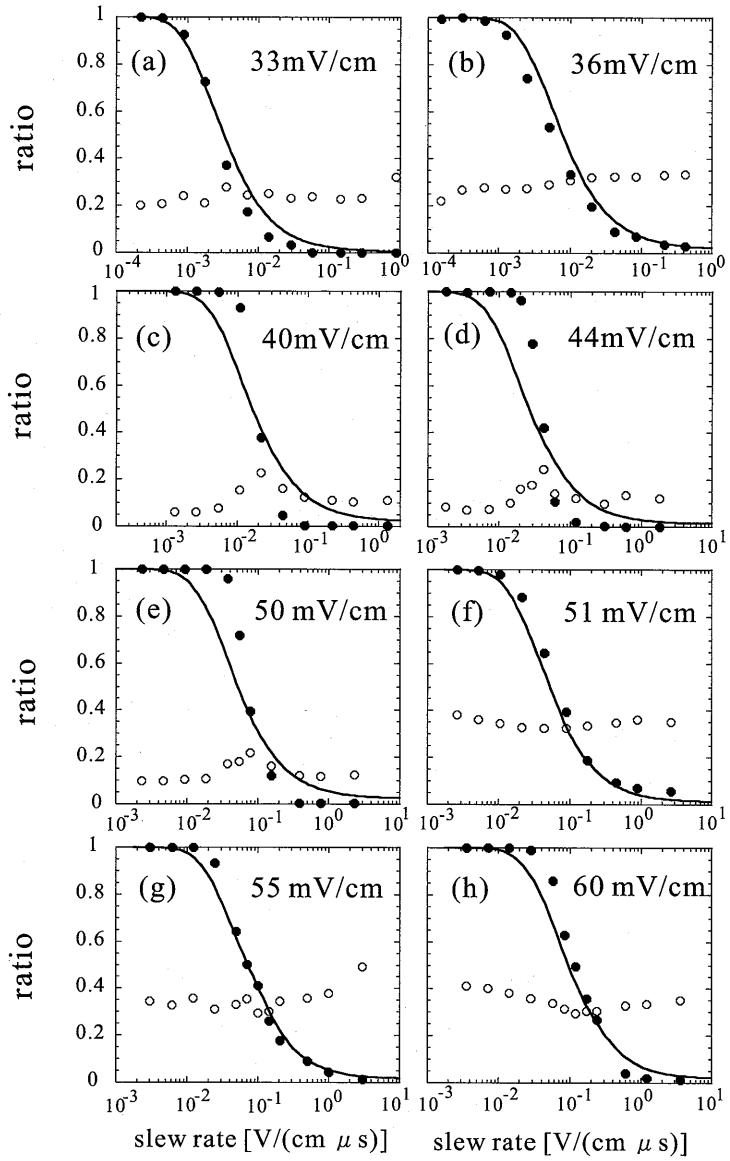

Figure 17: Slew rate dependence of the fractions of the tunneling and autoionization-like ionization signals with various values of F_r shown in each figure. Solid circles: experimental data from the tunneling ionization signals leading to the adiabatic path (the middle peak in Fig.15), open circles: experimental data from the autoionization signals (the lowest peak in Fig.15). Solid lines are quantum theoretical predictions based on the trace of the time evolution of the $113s_{1/2}$ state in the Stark energy map with m_j=1/2.

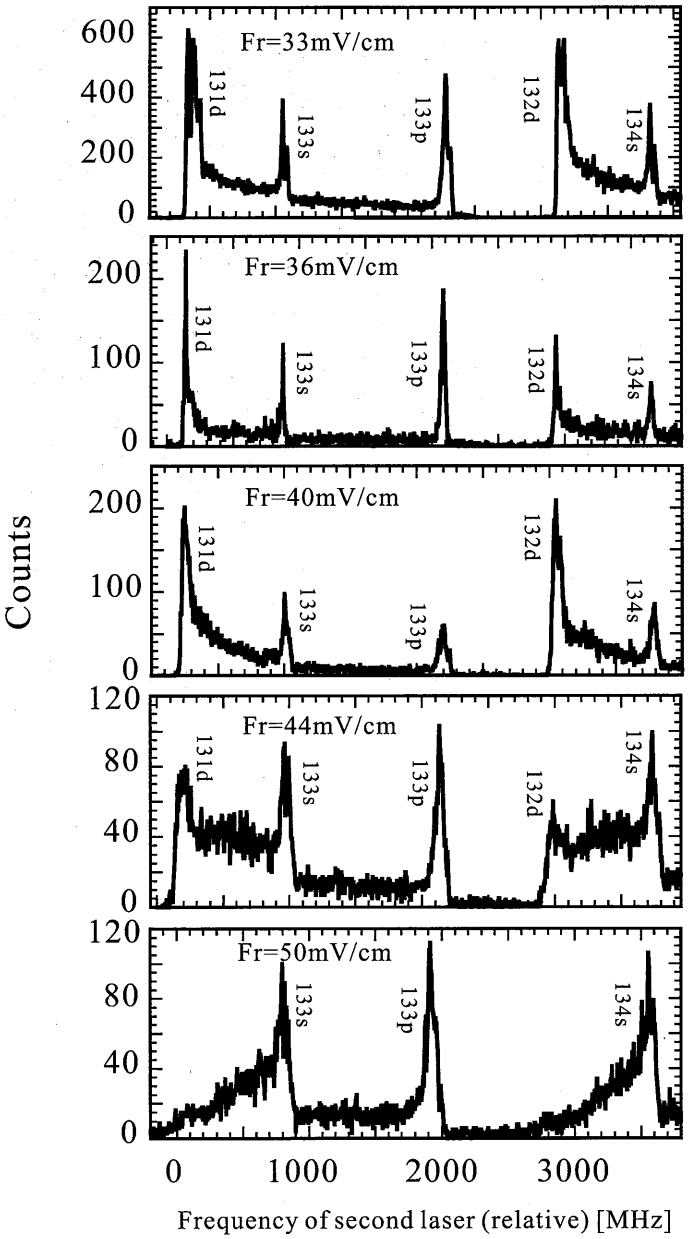

Figure 18: Laser excitation spectra of Rb Rydberg states around n=130 manifold with the electric field from 33 to 50 mV/cm. A series of this kind of spectra were measured to accurately determine the value of the electric field strength F_r, the field to which the $113s_{1/2}$ state is driven before the state is ionized with the following fast-rise pulsed field.

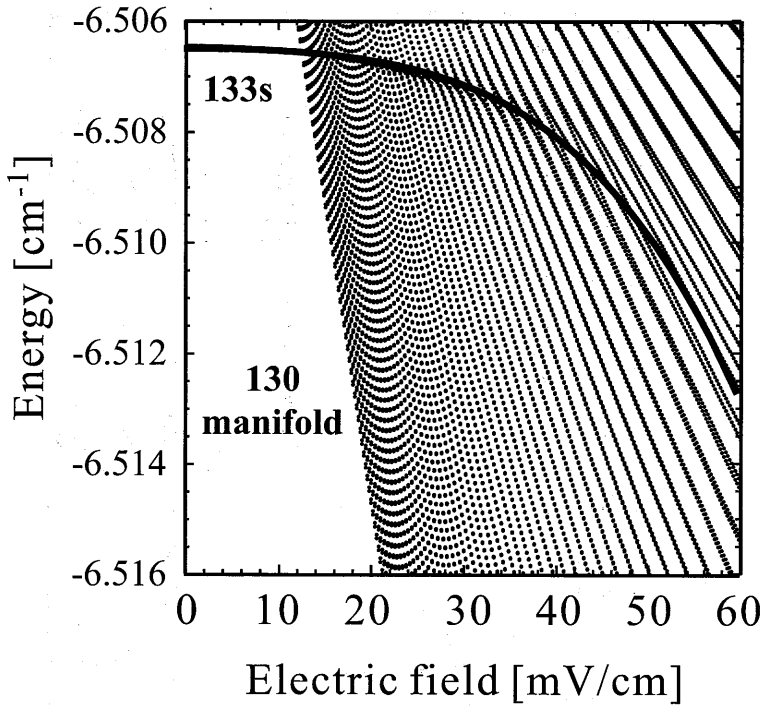

Figure 19: Part of the Stark energy map indicating the energy trajectory of the $133s_{1/2}$ state merged into the manifold states. From the comparison of this calculated trajectory with the experimentally observed peak of the s state, the electric field value F_r is accurately determined. See text for more detailed procedure on this determination.

is shown in Fig.19. Precise energy position of the s state is then evaluated by assuming that the s state has the maximum strengths of low ℓ components, that is, the components of s and d. The strengths of these components are obtained from the wave functions of each state near the $s_{1/2}$ trajectory, an example of which is shown in Fig.20. Overall accuracy in determining the F_r value with these processes is estimated to be within $\pm$ 1 mV/cm.

The value of the slew rate, at which the transition probability from adiabatic to diabatic paths becomes 0.5, is called transition slew rate S_{tr}. The F_r dependence of the value of S_{tr} is shown in Fig.21: The value S_{tr} increases abruptly from the threshold value, at which the $s_{1/2}$ state firstly avoided-crosses with the adjacent manifold, and then slowly increases with increasing F_r.

The above transition slew rate was determined with the observed ioniza-

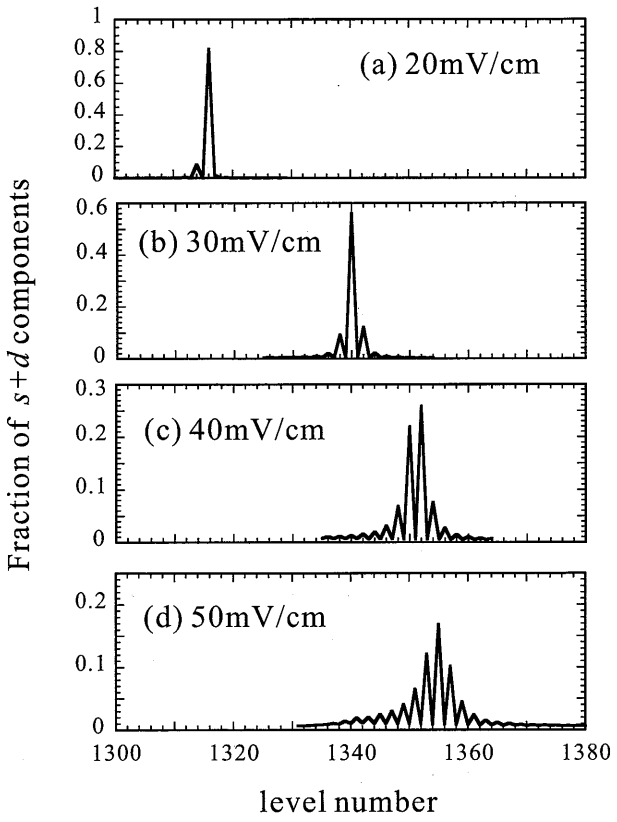

Figure 20: Fraction of the $(s + d)$ components in the wavefunction of the relevant states near the $130s$ state at the electric field shown in each figure. Horizontal axis shows the relative level-number of the relevant states taken into account in the evaluation of the wavefunctions. Center of the trajectory of the s state as a function of the applied electric field is determined from the center of these distributions of the components.

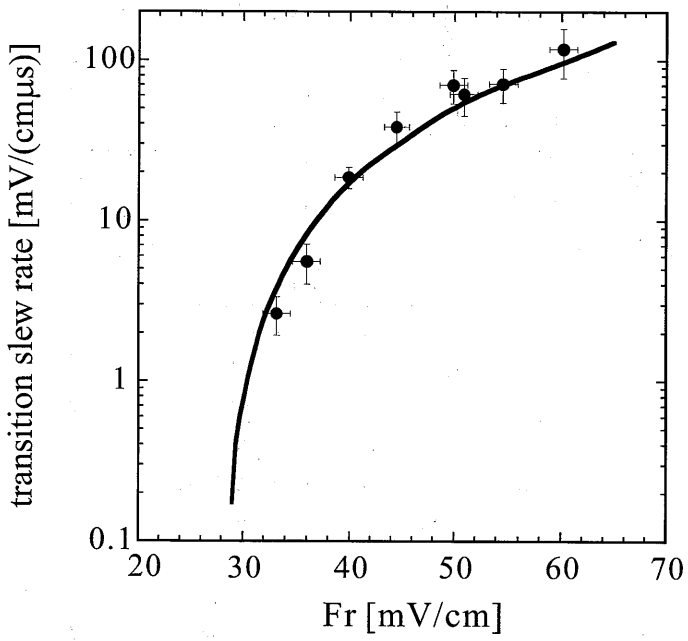

Figure 21: Dependence of the transition slew rate on the electric field F_r, to which the $113s_{1/2}$ state is driven before the subsequent field ionization pulse is applied. The transition slew rate here is the value of the slew rate at which the transition probability of the $s_{1/2}$ state to the adiabatic path is 50 %. Solid circles: experimental data, solid line: theoretical predictions. Errors of the data shown include both possible systematic errors arising from the determination of the electric field F_r and of the transition slew rate, and statistical ones.

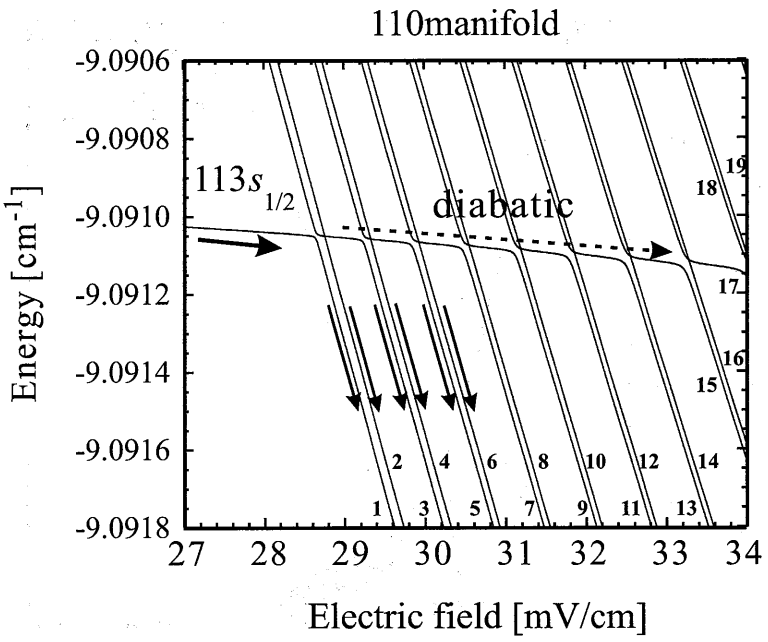

Figure 22: Stark energy map near the first avoided crossing of the $113s_{1/2}$ state with the adjacent n=110 manifold states. Possible transition paths in passing through these avoided crossings are shown with arrows together with the numbering of the relevant states. The diabatic path is shown with dashed line with arrow.

tion peaks from the tunneling processes. There is yet another peak coming from the autoionization-like process (AI in Fig.15). The fraction of this peak component to the total ionization signals was also shown in Fig.17 together with the ratio of the adiabatic to diabatic transitions from the tunneling processes. Although the fractions observed are rather insensitive to the slew rate, there is a small enhancement or reduction at the region of the transition slew rate throughout the observed data with varying F_r.

5.2 Theoretical predictions and comparison with experimental results

Following the prescription described in section3, we calculated the transitions at the first avoided crossings of $113s_{1/2}$ state with the adjacent manifold as a function of the value F_r. A Stark map relevant to these transitions is shown in Fig.22, where the splitting manifold levels are numbered from the

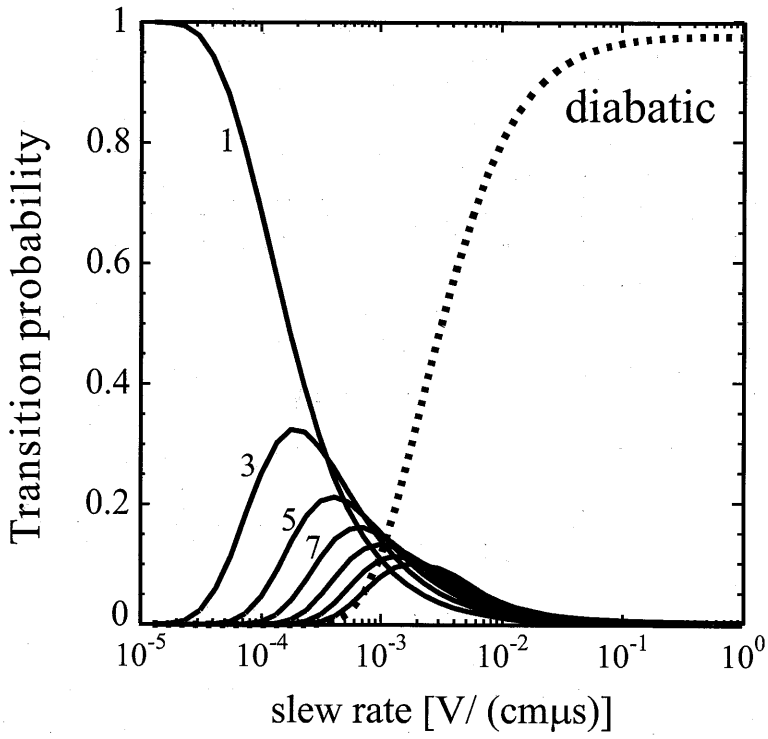

Figure 23: Transition probabilities of the initially populated $113s_{1/2}$ state at the well isolated Stark position from the manifold to the various states during the electric field driving as a function of the slew rate. The numbers shown in the figure indicate the state numbers labelled in Fig.22.

lower energy side.

The transition probabilities to these states calculated are shown in Fig.23 where the value of F_r is 33 mV/cm. Since the transitions to the states with even numbers are quite small, their contributions are omitted in the figure. The initial $s_{1/2}$ state transfers to the splitting manifold states intermediately and finally go through diabatically. From these calculated results, it was assumed that the ionization peak component corresponding to the adiabatic path (TU_a in Fig.15) includes all the contributions from these intermediate transitions. In fact it is clear that these intermediate contributions can not be resolved in the present limit of our experimental resolution. The theoretical predictions obtained are compared with the experimental results as shown in Figs.17 and 21. The transitional behavior is generally in good agreement with the experimental results as seen in Fig.21. However the theoretical

transition curves begins to decrease earlier than the experimental ones and ends to decrease more slowly with increasing slew rate. This diffusive trend in the transition region is more obvious in the intermediate values of F_r.

5.3 Discussions

In the previous two subsections, the experimental results on the transitions at the first avoided crossings of the $113s_{1/2}$ state with the adjacent n=110 manifold states were presented and quantum theoretical predictions were compared with the experiment. The predictions are generally in agreement with the experimental results. However, rather sharp transitions from the adiabatic to diabatic paths observed is not reproduced well by the predictions as stated above. The reason for this discrepancy is not known clearly but some of the possible effect might be the following: 1) Effect of a rotating electric field; In the theoretical calculations performed here, we took into account only the component of m_j=1/2 state throughout the whole time evolution. Underlying reasoning for this treatment is that since the time needed to increase the slow-component electric field from the initial to the final values F_r is not large, and also the field difference between this slow-component period is rather small, the initial substate m_j is maintained without redistribution due to the rotation of the electric field. In other words, the rotation of the elelctric field has its effect only during the period of steep rise of the subsequent field for the field ionization. Although the angle of rotation during the period of slow component is in fact small, less than 10 degrees, there might be some effect on the above discrepancy. 2) Effect of the component of the autoionization-like ionization process; Some constructive interference effects are seen in the fraction of the autoionization-like component at the values of F_r from 40 to 50 mV/cm (see Fig.17). In fact this enhancement seems to begin and end almost simultaneously with those of the theoretical transition behavior.

Related to the above feature in the autoionization-like process, it is interesting to note that the overall fraction of the component of the autoionization-like process have both contributions from the diabatic as well as adiabatic transition paths; This is because at the field of F_r, only the states near to the s trajectory (see Fig.22) must be populated and during the subsequent steep rise of the electric field, some fractions of the diabatic (path TU_d in Fig.15) and adiabatic (path TU_a in Fig.15) components proceed through the path AI, finally contributing the autoionization-like ionization. Since more than two paths contribute to this autoionization-like ionization process, some interference effect may be naturally expected to occur. In order to quantitatively analyze the above features, we need to do a theoretical simulation

study for the time evolution of the originally populated $113s_{1/2}$ state along the applied electric field to the point of ionization. Some progress along this line was already reported in [9].

Similar investigations on the transitions at the multilevel avoided crossings have been previously reported by Kishimoto[12]. The present study is an extension of his research by more explicitly controlling the experimental conditions on the transverse electric field, thus on the rotating electric field. The experimental results obtained in the present study are generally in agreement with his results.

As remarked in the Introduction, one of the aims of the present research is to get inevitable information required for the development of a stringently selective field ionization scheme at high Rydberg atoms: The essential ingredients of this scheme was reported in our previous publication[19]. In order to realize this scheme actually, we have to know precisely the transitional behavior of both of the $s_{1/2}$ and $p_{1/2,3/2}$ states along the adiabatic path through the reddest and bluest manifold states. The present results thus give important contributions for the above scheme to be applied to actual experiments such as a sensitive microwave single-photon detection with highly excited Rydberg atoms[19].

6 Conclusion

In conclusion we have clarified the transitional behavior of the $113s_{1/2}$ state at the first multilevel avoided crossings with the adjacent n=110 manifold states. Specifically the transitional behavior of the s state was measured as a function of the slew rate of the driving pulsed electric field. Special care has been taken during the course of the experiment to precisely measure the fractions of the ionization components through the tunneling processes by applying explicitly the transverse electric field, thus bringing the enhancement of the tunneling ionization process due to the effect of the rotating electric field. It was found by observing the fraction of the components of the tunneling ionization signals that the s state transfers to the reddest state of the adjacent n=110 manifold when the slew rate of the applied electric field is low enough (adiabatic passage), while with increasing slew rate, the state go through the diabatic path by partially passing some of the intermediate states in the splitting manifold states. These transitional behaviors are strongly dependent on how deep the s state is driven into the electric field where the state merges into the manifold states. Quantum theoretical predictions on these transitional behaviors, based on the numerical calculations of the time evolution of the relevant states in the Stark energy map, are in

good agreement with the experimental results.

In the field ionization spectra, a field ionization peak resulting from the autoionization-like process was also observed. The slew rate dependence of this component was found to be different from those of the tunneling ionization components mentioned above, indicating an interference effect between the possible ionization paths contributing to this process.

These findings provide us inevitable information to develop a stringently selective field ionization scheme for separately detecting the isolated s state from the neighboring p state[19, 20, 21, 22].

Acknowledgments

The author would like to express his thankfulness to Dr. Haruhiko Funahashi, Dr. Tomohito Haseyama, Mr. Chikara Ooishi, Mr. Tomoya Saida, Mr. Terunao Nakura and Prof. Katsuji Yamamoto.

The author would also like to express his deepest gratitude to Dr. Masaru Tada, Dr. Yasuhiro Kishimoto, Mr. Masahiro Shibata and Mr. Satoru Yamada, for their help and valuable discussions.

The special thanks should be offered to my academic adviser, Prof. Seishi Matsuki. His guide and suggestion were essential for this work.

References

[1] L. D. Landau, Phys. Z. Sowjetunion 2 (1932) 46.

[2] C. Zener, Proc. R. Soc. London, Ser. A 137 (1932) 696.

[3] N. A. Sinitsyn, Phys. Rev. B 66 (2002) 205303.

[4] V. A. Yurovsky, A. Ben-Reuven, P. S. julienne, Phys. Rev. A 65 (2002) 043607.

[5] J. R. Anglin, Phys. Rev. A 67 (2003) 051601(R).

[6] J. R. Rubbmark, M. M. Kash, M. G. Littman, D. Kleppner, Phys. Rev. A 23 (1981) 3107.

[7] T. Haseyama, K. Kominato, M. Shibata, S. Yamada, T. Saida, T. Nakura, Y. Kishimoto, M. Tada, I. Ogawa, H. Funahashi, K. Yamamoto, S. Matsuki, Phys. Lett. A 317 (2003) 450.

[8] Y. Kishimoto, M. Tada, M. Shibata, K. Kominato, S. Yamada, T. Haseyama, I. Ogawa, H. Funahashi, K. Yamamoto, S. Matsuki, Phys. Lett. A 303 (2002) 279.

[9] S. Yamada, Memoir of Faculty of Science, Kyoto University, Ser. Phys. Submitted.

[10] T. F. Gallagher, Rydberg Atoms, Cambridge University Press, Cambridge, 1994.

[11] V. A. Davydkin, B. A. Zon, Opt. Spectr. (USSR) 51 (1981) 13.

[12] Y. Kishimoto, Memoir of Faculty of Science, Kyoto University, Ser. Phys. 38 (2002) 163.

[13] M. Gross, J. Liang, Phys. Rev. Lett. 57 (1986) 3165.

[14] D. Delande, J. C. Gay, Europhys. Lett. 5 (1988) 303.

[15] J. Hare, M. Gross, P. Goy, Phys. Rev. Lett. 61 (1988) 1938.

[16] M. Cheret, F. Rousell, T. Bolzinger, G. Spiess, J. Hare, M. Gross, Europhys. Lett. 9 (1989) 231.

[17] R. Lutwak, J. Holley, P. P. Chang, S. Paine, D. Kleppner, T. Ducas, Phys. Rev. A 56 (1997) 1443, and references cited therein.

[18] L. Kristensen, E. Horsdal-Pedersen, P. Sorensen, J. Phys. B 31 (1998) 1049.

[19] M. Tada, Y. Kishimoto, M. Shibata, K. Kominato, S. Yamada, T. Haseyama, I. Ogawa, H. Funahashi, K. Yamamoto, S. Matsuki, Phys. Lett. A 303 (2002) 285.

[20] S. Matsuki, K. Yamamoto, Phys. Lett. 263 (1991) 523.

[21] I. Ogawa, S. Matsuki, K. Yamamoto, Phys. Rev. D 53 (1996) R1740.

[22] M. Tada, Y. Kishimoto, K. Kominato, M. Shibata, H. Funahashi, K. Yamamoto, A. Masaike, S. Matsuki, Nucl. Phys. B 72 (1999) 164.